

Stable p-Type Conduction from Sb-Decorated Head-to-Head Basal Plane Inversion Domain Boundaries in ZnO Nanowires

Andrew B. Yankovich,^{*,†} Brian Puchala,[†] Fei Wang,[‡] Jung-Hun Seo,[§] Dane Morgan,[†] Xudong Wang,[†] Zhenqiang Ma,[§] Alex V. Kvit,[†] and Paul M. Voyles[†]

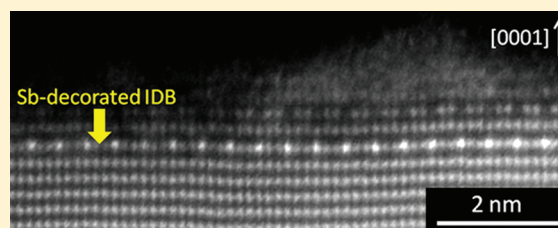
[†]Department of Material Science and Engineering, University of Wisconsin—Madison, Madison, Wisconsin 53706, United States

[‡]Department of Chemistry, University of Wisconsin—Madison, Madison, Wisconsin 53706, United States

[§]Department of Electrical and Computer Engineering, University of Wisconsin—Madison, Madison, Wisconsin 53706, United States

ABSTRACT: We report that Sb-decorated head-to-head (H–H) basal plane inversion domain boundaries (b-IDBs) lead to stable p-type conduction in Sb-doped ZnO nanowires (NWs) due to Sb and O codoping. Aberration-corrected Z-contrast scanning transmission electron microscopy shows that all of the Sb in the NWs is incorporated into H–H b-IDBs just under the (0001) NW growth surfaces and the (0001) bottom facets of interior voids. Density functional theory calculations show that the extra basal plane of O per H–H b-IDB makes them electron acceptors. NWs containing these defects exhibited stable p-type behavior in a single NW FET over 18 months. This new mechanism for p-type conduction in ZnO offers the potential of ZnO NW based p–n homojunction devices.

KEYWORDS: Zinc oxide (p-type), nanowire, Sb doping, inversion domain boundary, scanning transmission electron microscopy, density function theory



Doped semiconducting nanowires (NW) have unique properties that benefit a variety of nanoscale electronic and optoelectronic devices.^{1–3} ZnO is a promising material for UV optoelectronics due to its direct wide band gap of ~3.37 eV and large exciton binding energy of 60 meV,⁴ but the lack of a reliable p-type dopant due to low dopant solubility, native donor defects, and large acceptor ionization energies has restricted its use in optoelectronic applications.^{5–7} p-type ZnO thin films have been reported,^{8–15} but none of the results have been widely reproduced or resulted in stable optoelectronic devices. p-type ZnO NWs have also been reported^{16–19} but are similarly problematic. Doping with Sb is one of the reported methods of creating p-type films^{20–25} and NWs.²⁶ In particular, Sb-doped ZnO NWs grown on n-type ZnO thin films have been used to create electrically pumped waveguide lasers that are stable over 7 months.²⁷

We recently demonstrated p-type Sb-doped ZnO NWs synthesized and doped in solution,²⁶ which has the advantage of low cost and ease of processing. Here, we combine aberration-corrected scanning transmission electron microscopy (STEM) and density functional theory (DFT) calculations to elucidate the defects responsible for p-type conduction in solution-synthesized Sb-doped NWs. An overwhelming majority of the Sb in the NWs is incorporated into Sb-decorated head-to-head (H–H) (0001) basal plane inversion domain boundaries (b-IDBs) just under the (0001) NW growth surfaces and the (0001) bottom facets of interior voids. The H–H b-IDBs incorporate an extra basal plane of O compared to the ZnO host lattice, which, according to DFT calculations, makes them electron acceptors. This Sb and O

codoping renders the material p-type. We further show that the same NWs from our earlier report retain their p-type character 18 months after synthesis.

Sb-doped ZnO NWs were synthesized on silicon substrates with a ZnO seed layer grown from a zinc acetate ethanol solution.²⁶ The substrates were placed on the surface of a solution consisting of 25 mM sodium nitrate, 25 mM hexamethylenetetramine, and an Sb-dopant solution at 90 °C for 1 day to induce NW growth. The Sb-dopant solution consisted of sodium glycolate, created from equal molar sodium hydroxide and glycolic acid, and antimony acetate in a ratio of 12:1. Samples were treated with oxygen plasma to remove surface organics and then annealed in argon at 850 °C for 30 min to activate the p-type dopants.

Figure 1 shows the electrical transport behavior of a single Sb-doped ZnO NW field effect transistor (FET) showing clear p-type conduction. The FET consists of a single NW on a 100 nm SiO₂ dielectric on a heavily doped Si substrate which served as a back gate and Ti/Au source and drain contacts. The FET was passivated and sealed in 100 nm SiO₂ and 50 nm Si₃N₄. Measurements were made with a HP4155B semiconductor parameter analyzer. Further details of the NW fabrication and electrical measurements just after fabrication may be found in ref 26. Figure 1a,b shows electrical measurements of the same device 18 months later. Both as-synthesized and 18 months

Received: November 1, 2011

Revised: January 6, 2012

Published: January 23, 2012

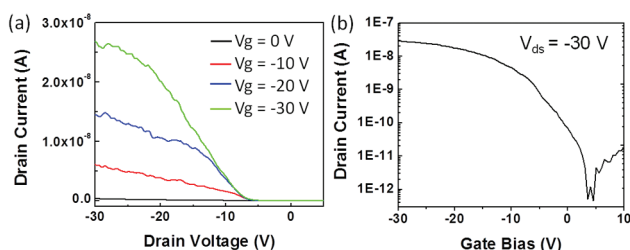


Figure 1. Single nanowire FET electrical measurements showing stable p-type character 18 months after fabrication. (a) Drain current vs drain voltage plots at various gate voltages, starting at 0 V and increased by -10 V steps to -30 V. (b) Drain current vs gate bias plot at a drain-source voltage of -30 V. Electrical data directly after fabrication showing p-type character can be found in ref 26.

later, the FET shows increasing source-drain current at more negative gate voltage, indicating p-type conduction.

Directly after fabrication, the NW had a field effect mobility of $1.2 \text{ cm}^2 \text{ V}^{-1} \text{ s}^{-1}$ and carrier concentration of $6.6 \times 10^{17} \text{ cm}^{-3}$,²⁶ derived from the NW FET geometry and electrical properties.²⁸ Eighteen months later, the same FET had a moderately reduced field effect mobility of $0.7 \text{ cm}^2 \text{ V}^{-1} \text{ s}^{-1}$ and carrier concentration of $1.2 \times 10^{17} \text{ cm}^{-3}$. The decrease in mobility and carrier concentration may indicate imperfect packaging of the FET, but the p-type character is stable. It is likely that the NWs are compensated, like most ZnO.²⁹ Separate concentrations of electrons and holes can be derived from temperature-dependent Hall effect data, as can bulk and surface contributions of the electrical behavior,³⁰ but that was not done on our NWs.

Atomic-resolution high angle annular dark field (HAADF) STEM was used to image the Sb-doped ZnO NWs. The HAADF image intensity scales as Z^α , where α is in the range 1.6–1.9 and Z is the atomic number of the atoms under the beam,³¹ although this can be altered by dynamical diffraction³² and strain.³³ This Z -contrast effect was used to distinguish the Zn and Sb atomic columns. STEM experiments were conducted on a FEI Titan microscope with a CEOS probe aberration corrector operated at 200 keV. HAADF STEM images were collected with a 24.5 mrad probe semiangle, 24.5 pA probe current, STEM resolution of $\sim 0.8 \text{ \AA}$, and HAADF detector range of 54–270 mrad. STEM samples were prepared by scratching NWs off the Si substrates with a fine needle onto nonporous 5 nm thick Si membrane window grids. Prior to STEM experiments, samples were plasma cleaned in a Fischione plasma cleaner in 25% oxygen–75% argon mixture for ~ 5 min to eliminate organic carbon surface contamination. The STEM images presented here were smoothed with a Gaussian smaller than the probe size to reduce noise.

Figure 2a,b shows atomic-resolution HAADF STEM images of different NWs with the $[0001]$ growth direction up in every image. Figure 2a is a $\langle 11\bar{2}0 \rangle$ projection of a NW tip, showing a terraced surface structure with Sb-decorated b-IBDs 2–3 planes under the (0001) growth surfaces, as marked by the yellow arrows. Because of the Z -contrast nature of the HAADF image and the difference in atomic number between O, Zn, and Sb, the pure O columns are invisible, and the Sb-containing atomic columns appear brighter than the regular Zn lattice atomic columns. The (0001) stacking sequence and atomic column positions across the IBD in this projection match previous reports of Sb-decorated b-IBDs in ZnO.^{34–37} Figure 2b is a $\langle 10\bar{1}0 \rangle$ projection of a NW tip, showing another Sb-decorated

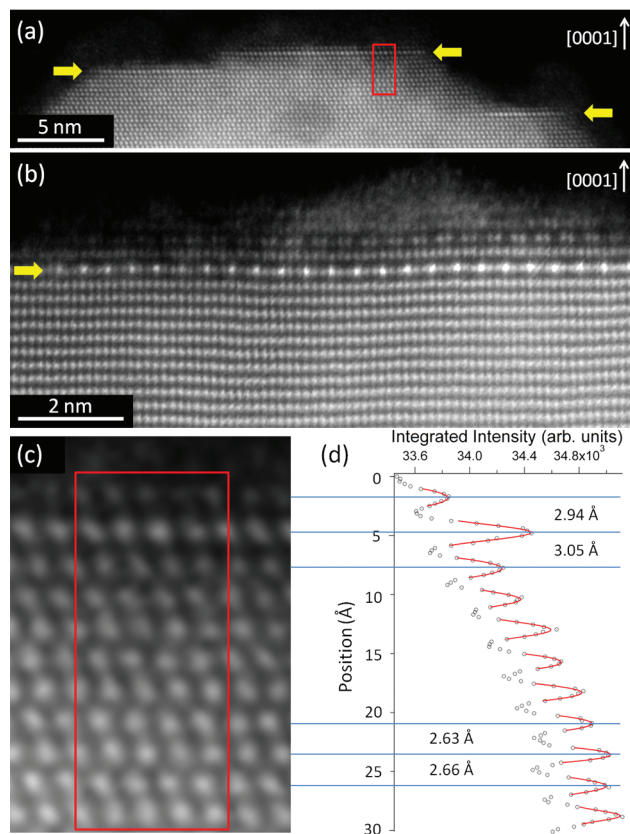


Figure 2. (a–c) HAADF STEM images with the growth direction up in every image. (a) and (b) are images of NW tips in the (a) $\langle 11\bar{2}0 \rangle$ and (b) $\langle 10\bar{1}0 \rangle$ projections, respectively, revealing Sb-decorated b-IBDs that are marked by yellow arrows. (c) Higher magnification image of the region surrounding the red box in (a). (d) Integrated line profile of the region inside the red box in (c), showing the lattice expansion around the IBD.

b-IBD that is marked with a yellow arrow. In this projection, the Sb-decorated (0001) plane has every third atomic column brighter, since in this projection pure Sb atomic columns are separated by two pure Zn atomic columns.^{34–37} Thus, in the $\langle 11\bar{2}0 \rangle$ projection image of Figure 2a, the atomic columns of the Sb-decorated (0001) plane are mixed Zn and Sb in the ratio of 2 to 1, explaining their lower contrast compared to the contrast of Sb atomic columns in Figure 2b.

Figure 2b shows a new ZnO (0001) surface reconstruction consisting of missing Zn atomic columns along $\langle 10\bar{1}0 \rangle$, stabilized by the Sb-decorated b-IBD. The surface is two Zn planes above the Sb-decorated b-IBD in Figure 2b. It consists of missing Zn atomic columns directly above the Sb columns in the b-IBD, separated by Zn dimer columns. Like a similar surface reconstruction of undoped ZnO with missing Zn atoms along $\langle 11\bar{2}0 \rangle$,³⁸ this structure eliminates 1/3 of the Zn atoms from the surface, stabilizing the ZnO polar (0001) surface by changing the surface stoichiometry. We believe missing Zn columns occur along $\langle 10\bar{1}0 \rangle$ instead of $\langle 11\bar{2}0 \rangle$ as previously reported due to strain from the larger Sb (compared to Zn) in the Sb-decorated b-IBD.

Figure 3a,c are HAADF STEM images showing the size and location of NW voids and internal b-IBDs. Figure 3a is a low-magnification image (with $[0001]$ growth direction pointing up) showing that the NWs have voids 2–20 nm in diameter at least 15–20 nm away from the NW side surfaces. TEM over/

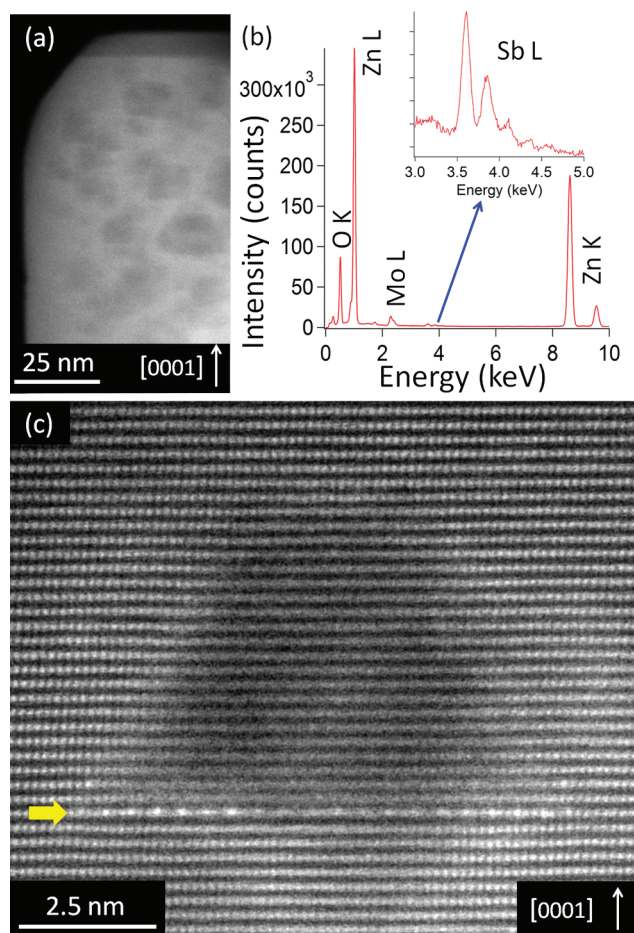


Figure 3. (a) Low-magnification HAADF STEM image of a NW showing the position and size of internal voids (the areas with darker contrast). [0001] growth direction points up in the image. (b) An integrated STEM EDS spectrum image of one NW revealing the presence of Sb with an Sb/Zn ratio of ~ 0.58 at %. (c) $\langle 10\bar{1}0 \rangle$ projection HAADF STEM image of a void showing an Sb-decorated H-H b-IDB marked with a yellow arrow just below the bottom facet of the void. The O-polar ZnO created by the H-H b-IDB is terminated after 2–3 monolayers by the voids bottom (0001) surface. As in Figure 2c, the lattice is expanded on either side of the IDB.

under focus images (not shown) showed the Fresnel fringe contrast reversal that confirms these features are voids.³⁹ Inside the NWs, the Sb-decorated b-IDBs sit just below the bottom (0001) facets of the voids, as marked by the yellow arrow in the $\langle 10\bar{1}0 \rangle$ projection image in Figure 3c. The b-IDBs terminate inside the NW, so even though they are not visible in our STEM images, partial dislocations must bound the planar b-IDBs around their edges. Figure 3c is a thicker part of the NW compared to Figure 2a,b, and the b-IDB does not penetrate through the entire thickness, so the contrast is lower than in Figure 2. Every NW we examined over multiple growth batches contained similar growth tips, voids, and b-IDBs.

The b-IDBs incorporate an overwhelming majority of the Sb present in the NWs. Figure 3b is an integrated STEM X-ray energy dispersive spectroscopy (EDS) spectrum image of one NW showing it contains Sb with an Sb/Zn ratio of ~ 0.58 at %, consistent with Wang et al.²⁶ STEM EDS near the edges of the NWs in regions without b-IDBs shows no Sb peak, although the poor counting statistics achievable without substantial beam damage limit the minimum detectable Sb fraction. However, we

have acquired Z-contrast STEM images of single substitutional and interstitial Sb atoms in Sb-doped thin films, and we have found no such features in any image of NWs. In total we searched $\sim 10^{-15}$ cm³ of NW thin edges and found no single Sb atoms, implying the concentration of substitutional Sb and Sb-containing point defect complexes is less than 10^{15} cm⁻³ and at least 2 orders of magnitude less than the measured carrier concentration. We therefore rule out the previously proposed mechanisms of substitutional Sb and Sb-containing point defect complexes^{40,41} as possible sources of p-type conductivity in these NWs.

There are two types of b-IDBs in ZnO, with the structures shown in Figure 4.^{34,37} Head-to-head (H-H) b-IDBs switch the

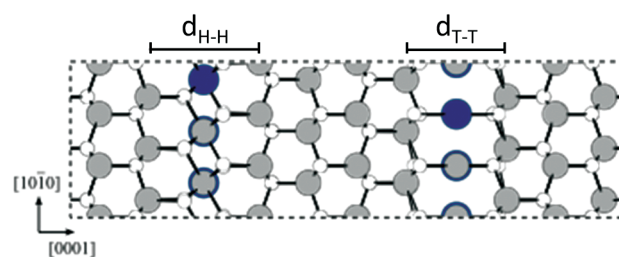


Figure 4. A DFT relaxed supercell structure containing both an H-H and T-T b-IDB with the stacking sequence AB(H-H)-A⁻¹C⁻¹A⁻¹C⁻¹(T-T)BAB, where -1 indicates planes of opposite polarity. Gray atoms are Zn. White atoms are O. Blue atoms are Sb in the b-IDB plane. Gray atoms with blue circles are Zn in the b-IDB plane.

polarity from Zn-polarity to O-polarity across the (0001) boundary, and tail-to-tail (T-T) b-IDBs switch the polarity from O-polarity to Zn-polarity. The H-H b-IDB incorporates an extra plane of O, creating octahedrally coordinated Zn and Sb in the defect plane. The T-T b-IDB is O-deficient, so the Zn and Sb remain tetrahedrally coordinated. We have calculated the relaxed structure and charge distribution of both b-IDBs using DFT,⁴² as implemented in the Vienna Ab Initio Software Package (VASP)^{43–47} and the Perdew, Burke, and Ernzerhof (PBE)^{48,49} generalized gradient approximation (GGA) exchange-correlation functional. We treated errors in the band gap of ZnO due to inadequate repulsion between Zn 3d and conduction band levels with the GGA+U correction,⁵⁰ and $U-J = 7.5$ eV⁵¹ so that the valence band and Zn 3d energy levels match experiment and self-interaction corrected calculations. We used a plane-wave energy cutoff of 600 eV and a $7 \times 5 \times 3$ Monkhorst–Pack k -point mesh.

The supercell in Figure 4 contains one H-H and one T-T b-IDB in order to satisfy periodic boundary conditions. The total stacking sequence is AB(H-H)A⁻¹C⁻¹A⁻¹C⁻¹(T-T)BAB, where -1 indicates planes of opposite polarity. In the relaxed structure, the H-H b-IDB causes a substantial lattice expansion, with a distance of $d_{\text{H-H}} = 5.95$ Å between the two (0001) Zn planes on either side of the defect, due to the larger size of the Sb ions and the extra O plane. The T-T b-IDB distance is $d_{\text{T-T}} = 5.38$ Å, and the undefected crystal c lattice parameter is 5.14 Å. We also relaxed a slab structure containing a single H-H b-IDB and a free surface, with the stacking sequence AB(H-H)A⁻¹C⁻¹. In the slab geometry the H–H basal plane spacing is $d_{\text{H-H}} = 6.04$ Å, in good agreement with the supercell geometry, indicating that the lattice expansion is not a result of nearby H-H and T-T b-IDBs interacting in the supercell.

The O sublattice is not visible in our Z-contrast STEM images so polarity cannot be directly determined, but comparison of the experimental and DFT calculated lattice spacing across the b-IDB plane shows that the NWs contain H-H b-IDBs. Figure 2c is part of a higher magnification STEM image corresponding to the red box in Figure 2a. Figure 2d is an integrated line profile of Figure 2c calculated from the raw (not smoothed) STEM image. The steady slope of the line profile is due to the NW thinning toward the tip. The peak of each atomic column profile was fit to a Gaussian to locate the maximum with subpixel accuracy. The Sb-decorated (0001) plane has a higher intensity compared to its neighbors and corresponds to the higher peak at 5 Å in the line profile. The b-IDB spacing, measured from the neighboring (0001) Zn planes, is 5.99 ± 0.04 Å. By doubling the average of the bottom five spacings, we get $c = 5.21 \pm 0.02$ Å as the average ZnO lattice parameter. The uncertainties are propagated from the uncertainties in the Gaussian center positions, estimated from the fit.

The experimental b-IDB spacing agrees with the DFT calculated $d_{\text{H-H}}$ from both the supercell and slab models. The experimental c lattice parameter agrees with previous experiments ($c = 5.207$ Å from Chen et al.⁴) and is only slightly larger than the DFT calculated c . Given the small disagreement with the ZnO lattice parameter, the outstanding agreement between STEM and DFT on the b-IDB H-H spacing is probably serendipity. However, the experimental uncertainties and the discrepancy in the c -axis lattice parameter are both significantly smaller than the difference in the simulated $d_{\text{H-H}}$ and $d_{\text{T-T}}$ of 0.57 Å, so the experiments definitively disagree with the smaller $d_{\text{T-T}}$. Other b-IDB images, such as Figure 3c, show similar lattice expansions around the b-IDB plane. Similar b-IDBs have been observed in bulk Fe-doped ZnO ceramics and In-doped ZnO NWs,^{52–54} as has a similar expanded 6.20 ± 0.30 Å lattice across the In-decorated H-H b-IDBs.

Figure 5 shows experimental and simulated position averaged convergent beam electron diffraction (PACBED) patterns

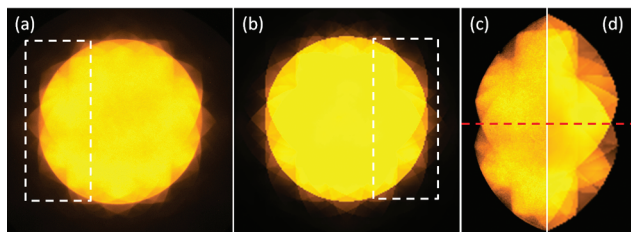


Figure 5. (a) Experimental PACBED pattern acquired near the edge of a NW away from voids and b-IDBs with the growth direction pointing up. (b) Simulated PACBED pattern of a 12.5 nm [1120] Zn-polar ZnO model using the frozen-phonon multislice algorithm. (c) and (d) Enlargements of the white dotted rectangles in (a) and (b), respectively. The match in asymmetry across the horizontal red dotted line in (c) and (d) show that, like the simulation, the NWs are Zn-polar.

demonstrating the NWs are Zn-polar ZnO. PACBED offers an accurate method of determining sample thickness⁵⁵ and polarity⁵⁶ through comparison of experimental and simulated patterns. Figure 5a is an experimental PACBED pattern acquired near the edge of a NW away from voids and b-IDBs with the growth direction pointing up. Figure 5b is a simulated PACBED pattern of Zn-polar ZnO using the Kirkland frozen-phonon multislice algorithm⁵⁷ and Debye–Waller factors for

ZnO from Reid,⁵⁸ averaged over one ZnO [1120] unit cell and 16 phonon configurations. A simulated sample thickness of 12.5 nm gives the best agreement with the experiment in Figure 5a. Figure 5c,d are enlargements of the white dotted rectangles in Figure 5a,b, respectively, contrast stretched to emphasize the polarity-induced PACBED asymmetry. Figure 5c,d show matching asymmetry across the horizontal red dotted line, demonstrating that, like the simulation, the NWs are Zn-polar. In addition to the large lattice expansion around the b-IDBs, these PACBED patterns provide evidence supporting the presence of H-H b-IDBs and not T-T b-IDBs.

Since we cannot isolate a single b-IDB in a periodic supercell, and the slab geometry has significant surface effects, it is not possible to directly explore the electronic levels of the b-IDB with DFT. However, we investigated the electrical activity of the b-IDBs indirectly by integrating the charge density within the Voronoi polyhedra surrounding each atom and assigning that net charge to the atom. Including the nuclear charge, H-H b-IDBs have a net negative charge of $-1.46e/\text{SbZn}_2\text{O}_6$ unit in the slab geometry and $-1.68e/\text{SbZn}_2\text{O}_6$ unit in the supercell geometry. T-T b-IDBs have a net positive charge of $+1.96e/\text{SbZn}_2$ (or $+1.62e/\text{SbZn}_8\text{O}_6$ if the neighboring planes are included in the T-T b-IDB) in the supercell geometry. These results indicate that H-H b-IDBs with excess O would act as acceptors and that T-T b-IDBs would act as donors, so a system containing more H-H b-IDBs would be net p-type, although not every electron captured by the H-H b-IDBs is likely to generate a free hole. This method of forming p-type ZnO is essentially O-doping of the material, where the doped O is stabilized by Sb codoping through the creation of stable Sb-decorated b-IDBs.

To the extent we can measure with STEM and PACBED, the NWs contain only H-H b-IDBs. This stands in contrast to bulk and thin film Sb-doped ZnO, which contains H-H b-IDBs, T-T b-IDBs, $\{10\bar{1}0\}$ IDBs, and $\{10\bar{1}1\}$ IDBs,⁵⁹ and to In-doped ZnO NWs, which contain H-H b-IDBs and $\{2\bar{1}\bar{1}5\}$ IDBs.⁵² If the NWs did not contain voids, they would need T-T b-IDBs or some other plane IDB to switch the ZnO polarity back to Zn-polar before there could be another H-H b-IDBs. The predominantly H-H character of the b-IDBs in our NWs may be explained by their appearance below the bottom (0001) facets of voids, as shown by Figure 3c. The O-polarity material created from the H-H b-IDBs is terminated after a few monolayers by the void's bottom (0001) surface. Zn-polar ZnO grows faster than O-polar ZnO,⁶⁰ so the Zn-polar material surrounding the b-IDBs topped with O-polar ZnO could overgrow the b-IDB region by forming a void over it. Further growth of the NW past the void is once again Zn-polar, so b-IDBs further up the wire are again H–H. We do not understand the lack of the $\{10\bar{1}0\}$ and $\{10\bar{1}1\}$ IDBs found in bulk and thin film Sb-doped ZnO, but we speculate that it is related to strain relief at the high density of surfaces in the NWs, at both interior voids and the NW surface. Having predominantly H-H b-IDBs leads to uncompensated holes and net p-type conduction. Incorporating the Sb into extended defects may make it, and the p-type conduction that results, more thermally stable, compared to doping with isolated impurities or metastable impurity–defect complexes.⁴⁰

The size and position of the voids in the NWs may be beneficial to the carrier concentration and mobility. The internal voids are small with respect to the NWs diameter, 2–20 nm compared to 50–120 nm, and the internal IDBs are the same size, covering only the base of the voids. (This is in

contrast to In-doped ZnO NWs, in which the b-IDBs span the whole width of the NWs.⁵²) Holes created by the H-H b-IDBs, therefore, do not have to move far to escape the extended defects and contribute to conduction. Moreover, conduction in ZnO NWs is dominated by surface conduction,^{61,62} and neither the voids nor IDBs are near the NW surface, so they should not significantly decrease the carrier mobility. The same scheme of creating holes through H-H b-IDBs separated from, but close to, high mobility conduction paths might be utilized to make p-type ZnO thin films by atomically abrupt delta doping with Sb.

In summary, aberration-corrected HAADF STEM shows that Sb-doped ZnO NWs contain Sb-decorated H-H b-IDBs just under the (0001) growth surfaces and the (0001) bottom facets of interior voids. DFT calculations reveal that the extra basal plane of O per H-H b-IDB acts as electron acceptors, explaining the p-type character of the ZnO NWs. This is a new mechanism for producing p-type character in ZnO, likely made possible by the NW morphology. The O and Sb-decorated b-IDBs are a stable configuration in the confined lattice of ZnO NWs, resulting in stable p-type conductivity over 18 months. This discovery suggests new possibilities for realizing ZnO based p-n homojunction devices.

ACKNOWLEDGMENTS

We acknowledge funding from the Department of Energy, Basic Energy Sciences (DE-FG02-08ER46547), Air Force of Scientific Research (FA9550-091-0482), and UW-NSF Nano-scale Science and Engineering Center (NSEC) (DMR-0425880).

REFERENCES

- Lauhon, L. J.; Gudixsen, M. S.; Lieber, C. M. *Philos. Trans. R. Soc. London, A* **2004**, *362*, 1247–1260.
- Huang, M. H.; Mao, S.; Feick, H.; Yan, H.; Wu, Y.; Kind, H.; Weber, E.; Russo, R.; Yang, P. *Science* **2001**, *292*, 1897–1899.
- Wang, Z. L.; Song, J. *Science* **2006**, *312*, 242–246.
- Chen, Y.; Bagnall, D. M.; Koh, H.-j.; Park, K.-t.; Hiraga, K.; Zhu, J. *J. Appl. Phys.* **1998**, *84*, 3912–3918.
- Yamamoto, T.; Katayama-Yoshida, H. *Physica B* **2001**, *302*–303, 155–162.
- Kohan, A.; Ceder, G.; Morgan, D.; Van de Walle, C. *Phys. Rev. B* **2000**, *61*, 15019–15027.
- Look, D.; Hemsky, J.; Sizelove, J. *Phys. Rev. Lett.* **1999**, *82*, 2552–2555.
- Su, S. C.; Yang, X. D.; Hu, C. D. *Physica B* **2011**, *406*, 1533–1535.
- Cheng, Y.-C.; Kuo, Y.-S.; Li, Y.-H.; Shyue, J.-J.; Chen, M.-J. *Thin Solid Films* **2011**, *519*, 5558–5561.
- Fan, J. C.; Zhu, C. Y.; Yang, B.; Fung, S.; Beling, C. D.; Brauer, G.; Anwand, W.; Grambole, D.; Skorupa, W.; Wong, K. S.; Zhong, Y. C.; Xie, Z.; Ling, C. C. *J. Vac. Sci. Technol., A* **2011**, *29*, 03A103.
- Joseph, M. J.; Tabata, H. T.; Kawai, T. K. *Jpn. J. Appl. Phys.* **1999**, *38*, L1205–L1207.
- Lu, J. G.; Ye, Z. Z.; Zhuge, F.; Zeng, Y. J.; Zhao, B. H.; Zhu, L. P. *Appl. Phys. Lett.* **2004**, *85*, 3134–3135.
- Chen, L. L.; Lu, J. G.; Ye, Z. Z.; Lin, Y. M.; Zhao, B. H.; Ye, Y. M.; Li, J. S.; Zhu, L. P. *Appl. Phys. Lett.* **2005**, *87*, 1–3.
- Rao, T. P.; Kumar, M. C. S. *J. Alloys Compd.* **2011**, *509*, 8676–8682.
- Kumar, E. S.; Chatterjee, J.; Rama, N.; DasGupta, N.; Rao, M. S. *ACS Appl. Mater. Interfaces* **2011**, *3*, 1974–1979.
- Wang, G.; Chu, S.; Zhan, N.; Zhou, H.; Liu, J. *Appl. Phys. A: Mater. Sci. Process.* **2011**, *103*, 951–954.
- Gupta, M. K.; Sinha, N.; Kumar, B. *J. Appl. Phys.* **2011**, *109*, 1–5.
- Xiang, B.; Wang, P.; Zhang, X.; Dayeh, S. a.; Aplin, D. P. R.; Soci, C.; Yu, D.; Wang, D. *Nano Lett.* **2007**, *7*, 323–328.
- Lu, M.-P.; Song, J.; Lu, M.-Y.; Chen, M.-T.; Gao, Y.; Chen, L.-J.; Wang, Z. L. *Nano Lett.* **2009**, *9*, 1223–1227.
- Aoki, T.; Shimizu, Y.; Miyake, A.; Nakamura, A.; Nakanishi, Y.; Hatanaka, Y. *Phys. Status Solidi B* **2002**, *229*, 911–914.
- Xiu, F. X.; Yang, Z.; Mandalapu, L. J.; Zhao, D. T.; Liu, J. L.; Beyermann, W. P. *Appl. Phys. Lett.* **2005**, *87*, 152101.
- Mandalapu, L. J.; Yang, Z.; Xiu, F. X.; Zhao, D. T.; Liu, J. L. *Appl. Phys. Lett.* **2006**, *88*, 1–3.
- Przeździecka, E.; Kamińska, E.; Pasternak, I.; Piotrowska, A.; Kossut, J. *Phys. Rev. B* **2007**, *76*, 1–4.
- Chu, S.; Lim, J. H.; Mandalapu, L. J.; Yang, Z.; Li, L.; Liu, J. L. *Appl. Phys. Lett.* **2008**, *92*, 1–3.
- Pan, X. H.; Guo, W.; Ye, Z. Z.; Liu, B.; Che, Y.; He, H. P.; Pan, X. Q. *J. Appl. Phys.* **2009**, *105*, 1–4.
- Wang, F.; Seo, J.-H.; Bayerl, D.; Shi, J.; Mi, H.; Ma, Z.; Zhao, D.; Shuai, Y.; Zhou, W.; Wang, X. *Nanotechnology* **2011**, *22*, 1–8.
- Chu, S.; Wang, G.; Zhou, W.; Lin, Y.; Chernyak, L.; Zhao, J.; Kong, J.; Li, L.; Ren, J.; Liu, J. *Nature Nanotechnol.* **2011**, *6*, 506–510.
- Goldberger, J.; Sirbully, D. J.; Law, M.; Yang, P. *J. Phys. Chem. B* **2005**, *109*, 9–14.
- Özgür, U.; Alivov, Y. I.; Liu, C.; Teke, A.; Reshchikov, M. a.; Doğan, S.; Avrutin, V.; Cho, S.-J.; Morkoç, H. *J. Appl. Phys.* **2005**, *98*, 1–103.
- Look, D. *Surf. Sci.* **2007**, *601*, 5315–5319.
- Hartel, P. *Ultramicroscopy* **1996**, *63*, 93–114.
- Hillyard, S.; Loane, R. F.; Silcox, J. *Ultramicroscopy* **1993**, *49*, 14–25.
- Perovic, D. D.; Rossouw, C. J.; Howie, A. *Ultramicroscopy* **1993**, *52*, 353–359.
- Rečnik, A.; Daneu, N.; Walther, T.; Mader, W. *J. Am. Ceram. Soc.* **2001**, *84*, 2657–2668.
- Shiojiri, M.; Recnik, A.; Yamazaki, T.; Kawasaki, M.; Ceh, M.; Watanabe, K. *Microsc. Microanal.* **2002**, *8*, 494–495.
- Yamazaki, T.; Nakanishi, N.; Recnik, A.; Kawasaki, M.; Watanabe, K.; Ceh, M.; Shiojiri, M. *Ultramicroscopy* **2004**, *98*, 305–316.
- McCoy, M. a.; Grimes, R. W.; Lee, W. E. *J. Mater. Res.* **2011**, *11*, 2009–2019.
- Torbrügge, S.; Ostendorf, F.; Reichling, M. *J. Phys. Chem. C* **2009**, *113*, 4909–4914.
- Ruhle, M.; Wilkens, M. *Cryst. Lattice Defects* **1975**, *6*, 129–140.
- Limpijumnong, S.; Zhang, S.; Wei, S.-H.; Park, C. *Phys. Rev. Lett.* **2004**, *92*, 1–4.
- Puchala, B.; Morgan, D. under review.
- Hohenberg, P.; Kohn, W. *Phys. Rev.* **1964**, *136*, 864–871.
- Kresse, G.; Hafner, J. *Phys. Rev. B* **1993**, *47*, 558–561.
- Kresse, G.; Hafner, J. *Phys. Rev. B* **1994**, *49*, 14251–14269.
- Kresse, G.; Furthmüller, J. *Comput. Mater. Sci.* **1996**, *6*, 15–50.
- Kresse, G.; Furthmüller, J. *Phys. Rev. B* **1996**, *54*, 11169–11186.
- Kresse, G.; Joubert, D. *Phys. Rev. B* **1999**, *59*, 1758–1775.
- Perdew, J. P.; Burke, K.; Ernzerhof, M. *Phys. Rev. Lett.* **1996**, *77*, 3865–3868.
- Perdew, J. P.; Burke, K.; Ernzerhof, M. *Phys. Rev. Lett.* **1997**, *78*, 1396.
- Anisimov, V. I.; Aryasetiawan, F.; Lichtenstein, A. I. *J. Phys.: Condens. Matter* **1997**, *9*, 767–808.
- Erhart, P.; Albe, K.; Klein, A. *Phys. Rev. B* **2006**, *73*, 1–9.
- Schmid, H.; Okunishi, E.; Oikawa, T.; Mader, W. *Micron* **2012**, *43*, 49–56.
- Yu, W.; Mader, W. *Ultramicroscopy* **2010**, *110*, 411–417.
- Wolf, F.; Freitag, B. H.; Mader, W. *Micron* **2007**, *38*, 549–52.
- LeBeau, J. M.; Findlay, S. D.; Allen, L. J.; Stemmer, S. *Ultramicroscopy* **2010**, *110*, 118–25.
- LeBeau, J. M.; D'Alfonso, A. J.; Wright, N. J.; Allen, L. J.; Stemmer, S. *Appl. Phys. Lett.* **2011**, *98*, 052904.
- Kirkland, E. J. *Advanced Computing in Electron Microscopy*, 1st ed.; Springer: Berlin, 1998.

- (58) Reid, J. S. *Acta Crystallogr., Sect. A* **1982**, *39*, 1–13.
- (59) Jo, W.; Park, C.; Kim, D.-Y. *Acta Crystallogr., Sect. A* **2007**, *63*, 229–233.
- (60) Park, J. S.; Chang, J. H.; Minegishi, T.; Lee, H. J.; Park, S. H.; Im, I. H.; Hanada, T.; Hong, S. K.; Cho, M. W.; Yao, T. *J. Electron. Mater.* **2007**, *37*, 736–742.
- (61) Li, Q. H.; Wan, Q.; Liang, Y. X.; Wang, T. H. *Appl. Phys. Lett.* **2004**, *84*, 4556–4558.
- (62) Chen, C.-Y.; Chen, M.-W.; Ke, J.-J.; Lin, C.-A.; Retamal, J. R. D.; He, J.-H. *Pure Appl. Chem.* **2010**, *82*, 2055–2073.